www.sciencemag.org/cgi/content/full/329/5987/69/DC1

Supporting Online Material for

# Experimental Results for $H_2$ Formation from $H^-$ and H and Implications for First Star Formation

H. Kreckel,* H. Bruhns, M. Čížek, S. C. O. Glover, K. A. Miller, X. Urbain, D. W. Savin

*To whom correspondence should be addressed. E-mail: hkreckel@illinois.edu

Published 2 July 2010, *Science* **329**, 69 (2010)
DOI: 10.1126/science.1187191

**This PDF file includes:**

# Supporting Online Material for

## Experimental Results for $H_2$ Formation from $H^-$ and H and Implications for First Star Formation

H. Kreckel, H. Bruhns, M. Čížek, S. C. O. Glover,
K. A. Miller, X. Urbain, D. W. Savin

## Experimental uncertainties and resolution

### Experimental uncertainties

The error bars given in Fig. 2 represent the statistical uncertainty of the measurement derived from the accumulated $H_2^+$ count rate at each data point. In our measurement scheme the $H^-$ and H beams are chopped out of phase with one another to reduce beam related backgrounds (*S1*). The statistical error shown in Fig. 2 is proportional to the propagated $1\sigma$ uncertainty of the $H_2^+$ count rate after background subtraction. The center-of-mass collision energy range from 3.7 meV to 1 eV was divided into two overlapping energy regions (3.7 meV to 0.11 eV and 0.086 eV to 1 eV, respectively). The low energy region was measured 3 times. The high energy region – yielding lower count rates – was measured 8 times. Typically a few hundred $H_2^+$ counts were accumulated for each data point in a given measurement.

The systematic error is dominated by the uncertainty of the $H_2$ stripping cross section in helium. We adopt the measured cross section value of $\sigma_{\mathrm{st}} = 1.04 \times 10^{-16}\,\mathrm{cm}^2$ with an uncertainty of 16.5% from Browning *et al.* (*S2*). In (*S2*) the $H_2^+$ yield from a neutral He atom beam traversing $H_2$ gas was measured. Taken at the appropriate relative velocity this corresponds to the same collision process that takes place inside our helium gas cell. An additional uncertainty is introduced by the fact that the $H_2$ molecules produced by the AD process in our experiment are likely to be ro-vibrationally excited, however, we do not expect a dramatic effect on the stripping cross section.

Bouliou *et al.* (*S3*) have measured the stripping cross section of vibrationally excited $H_2$ in helium in a relative measurement. In (*S3*) $H_2^+$ ions were created in a discharge ion source and neutralized in a gas cell, yielding fast $H_2$ molecules. The ro-vibrational states populated for $H_2^+$ ions produced in discharge and electron impact ion sources typically show a distribution in agreement with calculated Franck-Condon factors (*S4, S5*). Starting with this distribution and using Franck-Condon factors to calculate the vibrational levels populated by electron transfer in collisions of $H_2^+$ with a gas target, we find that the final $H_2$ has a broad distribution of vibrational levels. Our calculations also show that the internal states populated in $H_2$ molecules produced by the AD process are expected to populate a similarly broad distribution. The stripping cross section measured by Bouliou *et al.* agrees well with the measurement of Browning *et al.* (see Fig. S1). However, since the measurements of Bouliou *et al.* are relative measurements that had to be normalized to the $H_2$ on $H_2$ stripping cross section of McClure (*S6*) and since no

discussion of the uncertainties is given in Bouliou *et al.*, we use the well-documented cross section measured by Browning *et al.* as our reference value.

Complementary information can be derived from the measurements of Tabet *et al.* which were performed with a fast $H_2$ beam traversing a helium cell at higher energies (100 keV to 120 keV). Figure S1 shows a comparison of the experimental data up to 120 keV. The results of Tabet *et al.* confirm those of Bouliou *et al.* Taking into account the published work of (*S2,S3,S7*) leads us to conclude that the internal excitation of the $H_2$ molecules does not have a significant influence on the stripping process.

To get a quantitative estimate of the uncertainty induced by the unknown internal excitation we consider the stripping cross sections of fast $H_2$ molecules traversing $H_2$ gas, measured by Williams *et al.* (*S8*). In their experiment $H_2^+$ beams were produced from two different ion sources and neutralized in a gas cell to create a beam of fast $H_2$ molecules. In order to manipulate the internal energy of the $H_2$ molecules the discharge current in each ion source was varied by two orders of magnitude and the pressure was changed over four orders of magnitude. The change in the measured cross sections was up to 10%. We include this value as an additional uncertainty for our absolute value. Added quadratically with minor error sources such as the ion and neutral beam current measurements and the detector efficiency, our total systematic uncertainty at an estimated $1\sigma$ level amounts to 25%.

**Energy resolution**

The experimental center-of-mass collision energy resolution is influenced by two parameters: the energy spread of the ion source and the angular spread of the overlapping beams. The latter domintates the resolution at low collision energies. The energy spread of the ion source is assumed to be 10 eV, based on a beam modulation measurement determining the time of flight distribution by chopping the $H^-$ beam with one of the steerer electrodes. The energy spread agrees with previously published values for the same type of ion source (*S9*). The angular spread is constrained by two 5 mm apertures that are located before and after the photodetachment region, 2.8 m apart. We have written a geometric simulation that takes both effects into account. Figure S2 shows the simulated center-of-mass collision energy as a function of the voltage applied to the drift tube that is used to adjust the relative beam velocities. The black dots denote the mean value of the simulated center-of-mass collision energy distribution, the error bars display the root mean square of the distribution.

# Thermal rate coefficient and comparison to previous results

**Thermal rate fit**

Figure S3 shows the thermal rate coefficient for the AD reaction

$$H^- + H \rightarrow H_2 + e^-.$$

The solid dots are the result of our extended cross section calculation based on the method developed in (*S10*). To convert the cross section into a thermal rate coefficient it has been multiplied with the relative velocity and convolved with a Maxwell-Boltzmann velocity distribution. The black line is a plot of the analytical fit given in Table S1. The fit reproduces the calculation to better than 3% for the temperature range of $10^{-1}$ to $10^{5}$ K. Based on the good agreement with the experimental results we recommend this fit for the thermal rate coefficient of the AD reaction. We estimate an absolute $1\sigma$ uncertainty of 25% as derived from the systematic uncertainty of the experiment.

**Previous experimental and theoretical results**

Previous experimental studies of the AD process were carried out in flowing afterglows at room temperature (300 K). Since these experiments sample a thermal ensemble, they cannot be compared directly to our merged beams results. To be able to distinguish between them we plot the results of Schmeltekopf *et al.* (*S11*), Fehsenfeld *et al.* (*S12*), and Martinez *et al.* (*S13*) as black squares in Fig. S3 at 250 K, 300 K, and 350 K, respectively. The Langevin rate constant is plotted as a dashed black line. Note that in this case the classical Langevin collision rate coefficient has been divided by a factor of two. While the collision at low energies can proceed along the $^2\Sigma_u^+$ and the $^2\Sigma_g^+$ surfaces with equal probability, only the attractive $^2\Sigma_u^+$ potential is expected to contribute to the AD process. The theoretical results of Browne and Dalgarno for two different potentials are represented by red solid and dashed lines, respectively (*S14*). The calculations of Sakimoto are shown as a blue line (*S15*). The calculations of Launay *et al.* for two different potentials are shown as green solid and dashed lines, respectively (*S16*).

# Cosmological simulation

**Implementation details**

The hydrodynamical simulations described in the paper were performed using a modified version of the GADGET 2 smoothed particle hydrodynamics (SPH) code (*S17*). Our modifications involve the addition of a treatment of primordial chemistry and the corresponding atomic and molecular cooling processes to the code, along with a scheme for replacing gas in unresolved regions with collisionless "sink" particles (*S18, S19*). Our treatment of the metal-free chemistry is based on (*S20*), but we have updated a number of the reaction rate coefficients to match the values used in (*S21*). We adopt case B rate coefficients for the recombination of $H^+$ and $He^{++}$ and treat $He^+$ recombination as described in Section 2.1.4 of (*S21*). For the mutual neutralization of $H^-$ by $H^+$ (reaction 5 in (*S20*)), we use the rate coefficient given by (*S22*), which recent calculations suggest is the most reliable (*S23*). The rate coefficient for the associative detachment of $H^-$ ions by atomic hydrogen is varied from run to run, as discussed in the main text.

Our treatment of the gas cooling follows the description in (*S21*). In particular, we note the importance of including the effects of $H_2$–$H^+$ and $H_2$–$e^-$ collisions when computing the total

$H_2$ cooling rate, as highlighted in (*S21*), since these collisional processes dominate when the fractional ionization of the gas is large.

We create sink particles following the prescription described in (*S19*), and adopt a threshold density for sink formation of $n_{\rm th} = 10^6 \, {\rm cm}^{-3}$. The sink accretion radius is taken to be $r_{\rm sink} = 0.15 \, {\rm pc}$. In practice, the fact that we compare the different simulations at a time just prior to the formation of the first sink particle in each case means that the details of the sink particle algorithm have no influence on the outcome.

**Initial conditions**

We use initial conditions similar to those from (*S24*) which were adopted for our earlier study of the potential importance of uncertainties in the associative detachment and mutual neutralization rate coefficients. Closely related initial conditions were also used more recently by (*S25, S26*) for the study of the effects of metal enrichment in initially ionized cosmological minihalos. We consider a minihalo with a total mass of $9.7 \times 10^5 \, {\rm M}_\odot$ and a baryonic mass of $2 \times 10^5 \, {\rm M}_\odot$, present at a redshift $z = 25$. We assume that the gas is initially fully ionized, with a uniform temperature of $10^4 \, {\rm K}$, being maintained in this state by some external source of radiation, such as a distant Population III star or miniquasar (see (*S27*), where a similar setup is used). The virial temperature of the minihalo is $2200 \, {\rm K}$, and so the $10^4 \, {\rm K}$ gas can settle into hydrostatic equilibrium in the potential well created by the minihalo, and does not undergo runaway collapse. At the beginning of the simulation, we assume that the external ionizing source switches off, as would happen, for example, if the Population III star reached the end of its life. Therefore, during the simulation, the gas is free to recombine, cool, and undergo runaway gravitational collapse into the center of the minihalo. For simplicity, we represent the dark matter in the minihalo using a fixed background gravitational potential, which we take to be a standard Navarro-Frenk-White potential (*S28*). Since here we are not interested in small-scale features of the dark matter gravitational potential, such as any potential substructure, this simplifying assumption is justified. We adopted cosmological parameters taken from the WMAP 5th year analysis (h = 0.71, $\Omega_b$ = 0.046, $\Omega_m$ = 0.27, $\sigma_8$ = 0.81; see (*S29*) for more details), but we note that we do not expect our results to be sensitive to this choice.

We use two million SPH particles to represent the gas, giving us a particle mass of $0.1 \, {\rm M}_\odot$ and a mass resolution of $10 \, {\rm M}_\odot$. For gas at the threshold density for sink particle formation, and at the CMB temperature $T_{\rm CMB} \simeq 70 \, {\rm K}$, the Jeans mass is $40 \, {\rm M}_\odot$ (*S19*), and so we can be certain that the Jeans mass remains resolved throughout our simulation.

We adopt a He/H ratio of 0.079 and a D/H ratio of $2.6 \times 10^{-5}$ with both ratios given by number (*S30*). We assume that the gas is initially fully ionized, with $x_{\rm H^+} = 1.0$, $x_{\rm He^+} = 0.079$, and $x_{\rm D^+} = 2.6 \times 10^{-5}$ (where $x_i$ denotes the fractional abundance of chemical species $i$ relative to the abundance of H nuclei in all forms). The initial abundances of all other species are set to zero.

**Analysis**

The simulations were run until shortly after the formation of a central sink particle, but in

order to ensure that our sink particle algorithm would not affect the results of the comparison, we chose to analyze the runs at a point immediately prior to sink particle formation. Because the choice of AD rate coefficient can affect the time required for the gas to collapse by up to 50%, we did not compare results at the same output time, but rather compared results at the same evolutionary stage, measured by the total hydrogen nuclei number density of the gas in the center of the halo. To generate the plots shown in Fig. 3, we computed the average values of density, temperature, and $H_2$ and HD abundances within a large set of concentric, spherical shells, centered on the densest portion of the simulation, and with widths that increase logarithmically as one moves outwards. The increasing scatter seen in the plots as we move to higher density is a consequence of the fact that these shells are close to the center of the halo and contain fewer SPH particles than the shells that are further out.

# References


S1. H. Bruhns *et al.*, *Rev. Sci. Instrum.* **81**, 013112 (2010).

S2. R. Browning, C. J. Latimer, H. B. Gilbody, *J. Phys. B* **3**, 667 (1970).

S3. A. Bouliou, M. Sarret, P. Frere, *C.R. Acad. Sc. Paris* **296II**, 1377 (1983).

S4. F. Von Busch, G.H. Dunn, *Phys. Rev. A* 5, 1726 (1972).

S5. S. Krohn *et al.*, *Phys Rev. A.* **62**, 032713 (2000).

S6. G.W. McClure, *Phys. Rev*, **134**, A1226 (1964).

S7. J. Tabet, S. Eden, F. Gobet, B. Farizon, M. Farizon, S. Ouaskit, P. Scheier, T.D. Märk, *Int. J. Mass Spectrom.*, **272**, 48 (2008).

S8. I. D. Williams, J. Geddes, H. B. Gilbody, *J. Phys. B* **17**, 811 (1984).

S9. C. C. Havener, M. S. Huq, H. F. Krause, P. A. Schulz, R. A. Phaneuf, *Phys. Rev. A* **39**, 1725 (1989).

S10. M. Čížek, J. Horáček, W. Domcke, *J. Phys. B* **31**, 2571 (1998).

S11. A. L. Schmeltekopf, F. C. Fehsenfeld, E. E. Ferguson, *Astrophys. J.* **148**, L155 (1967).

S12. F. C. Fehsenfeld, C. J. Howard, E. E. Ferguson, *J. Chem. Phys.* **58**, 5841 (1973).

S13. O. Martinez, Jr., Z. Yang, N. B. Betts, T. P. Snow, V. M. Bierbaum, *Astrophys. J.* **705**, L172 (2009).

S14. A. Browne, A. Dalgarno, *J. Phys. B.* **2**, 885 (1967)

S15. K. Sakimoto, *Chem. Phys. Lett* **164**, 294 (1989)

S16. J. M. Launay, M. Le Dourneuf, C. J. Zeippen, *Astron. Astrophys.* **252**, 842 (1991)

S17. V. Springel, *Mon. Not. R. Astron. Soc.* **364**, 1105 (2005).

S18. M. R. Bate, I. A. Bonnell, N. M. Price, *Mon. Not. R. Astron. Soc.* **277**, 362 (1995).

S19. A.-K. Jappsen, R. S. Klessen, R. B. Larson, Y. Li, M.-M. Mac Low, *Astron. Astrophys.* **435**, 611 (2005).

S20. S. C. O. Glover, A.-K. Jappsen, *Astrophys. J.* **666**, 1 (2007).

S21. S. C. O. Glover, T. Abel, *Mon. Not. R. Astron. Soc.* **388**, 1627 (2008).

S22. H. Croft, A. S. Dickinson, F. X. Gadea, *Mon. Not. R. Astron. Soc.* **304**, 327 (1999).

S23. M. Stenrup, Å. Larson, N. Elander, *Phys. Rev. A* **79**, 012713 (2009).

S24. S. C. Glover, D. W. Savin, A.-K. Jappsen, *Astrophys. J.* **640**, 553 (2006).

S25. A.-K. Jappsen, S. C. O. Glover, R. S. Klessen, M.-M. Mac Low, *Astrophys. J.* **660**, 1332 (2007).

S26. A.-K. Jappsen, M.-M. Mac Low, S. C. O. Glover, R. S. Klessen, S. Kitsionas, *Astrophys. J.* **694**, 1161 (2009).

S27. B. W. O'Shea, T. Abel, D. Whalen, M. L. Norman, *Astrophys. J.* **628**, L5 (2005).

S28. J. F. Navarro, C. S. Frenk, S. D. M. White, *Astrophys. J.* **490**, 493 (1997).

S29. E. Komatsu *et al.*, *Astrophys. J. Suppl. Ser.* **180**, 330 (2009).

S30. R. H. Cyburt, *Phys. Rev. D* **70**, 023505 (2004).

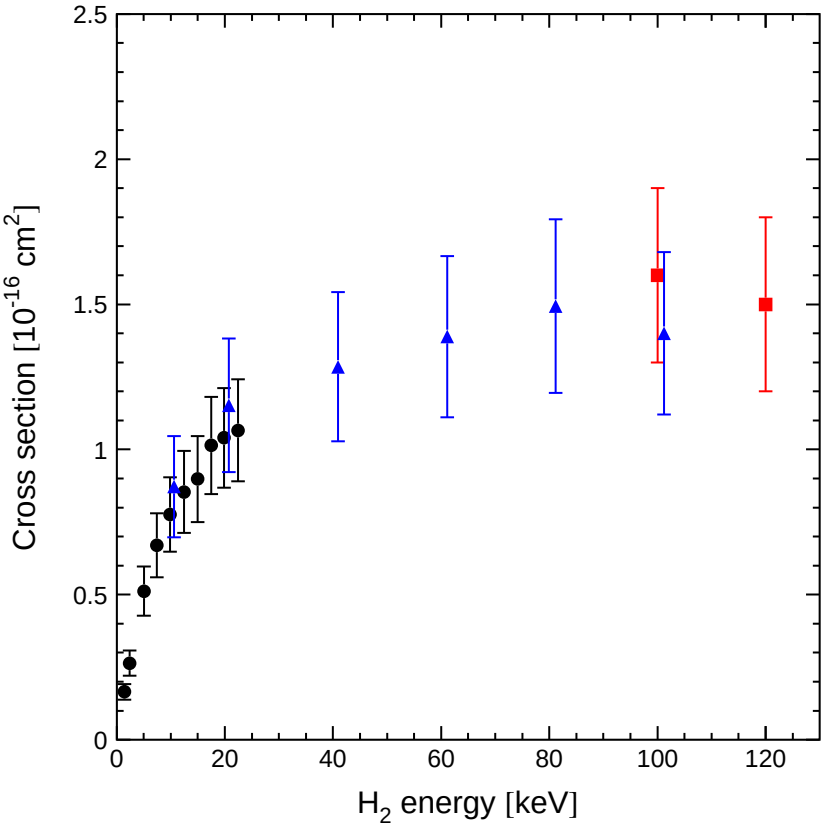


Figure S1: Experimental results for the electron stripping of $H_2$ in helium. The black dots depict the measurements of Browning *et al.* (*S2*), the blue triangles the measurements of Bouliou *et al.* (*S3*) and the red squares show the measurements of Tabet *et al.* (*S7*). Here we have followed the work of Tabet *et al.* (*S7*) and assumed a 20% uncertainty for the results of Bouliou *et al.*

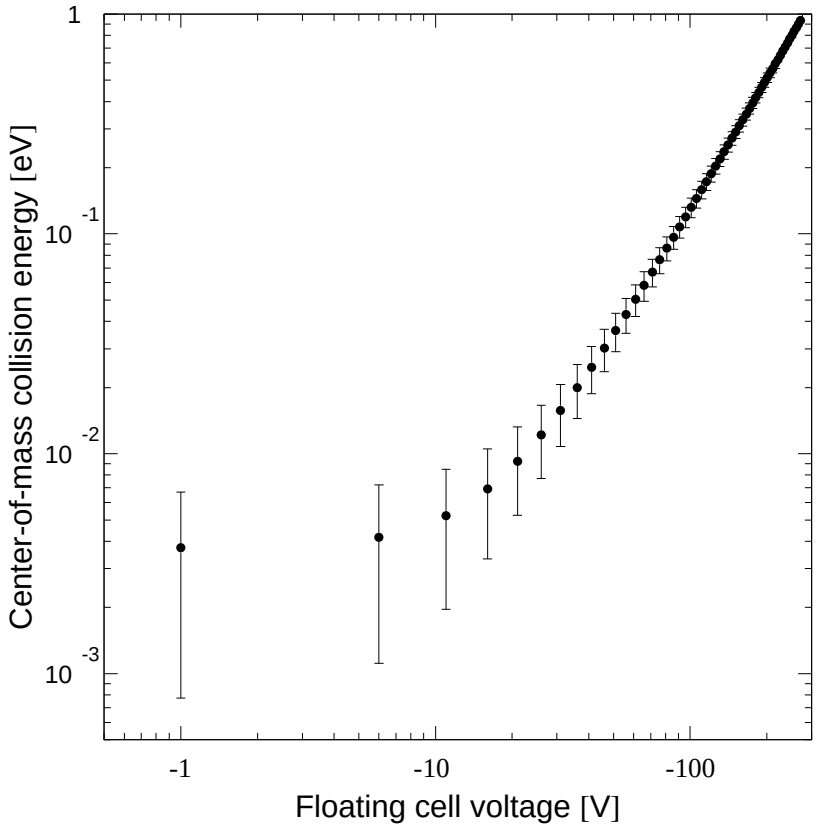


Figure S2: Simulated center-of-mass collision energy as a function of the voltage applied to the drift tube that is used to control the relative beam energies. The black dots denote the mean value of the simulated collision energy distribution, the error bars display the root mean square of the distribution.

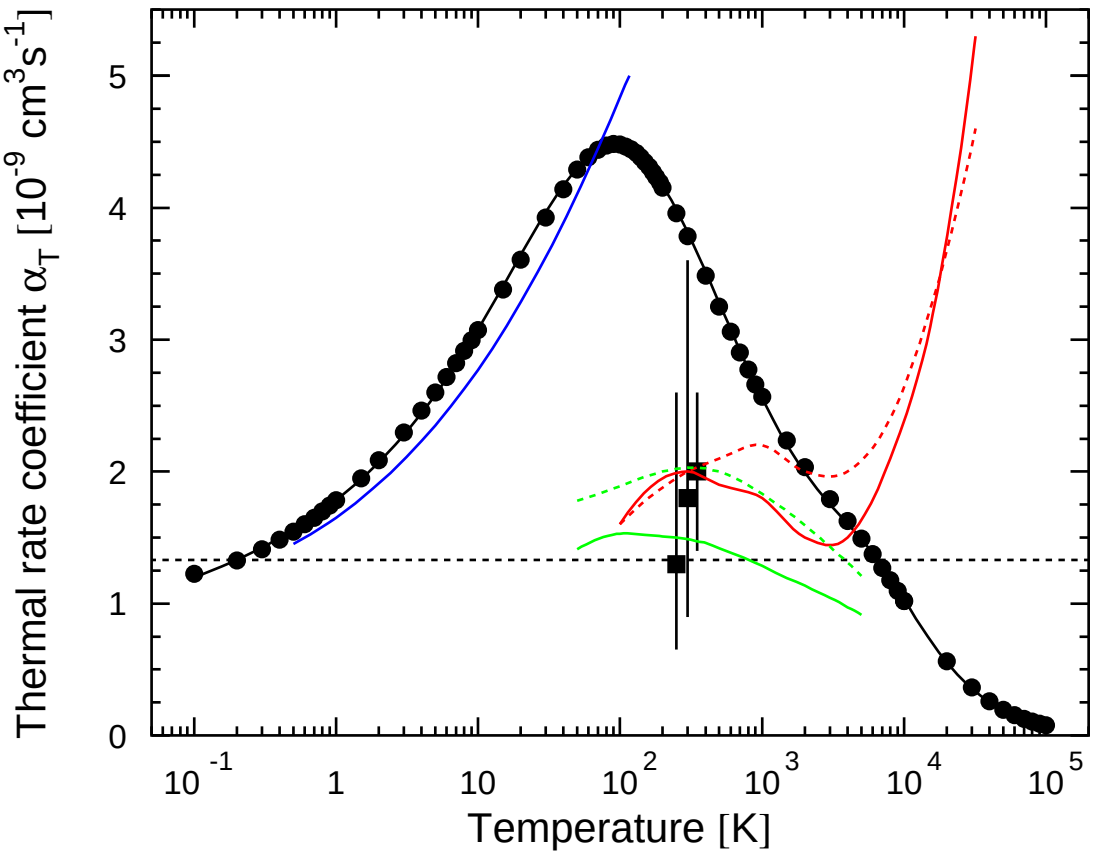


Figure S3: Thermal rate coefficient $\alpha_{\mathrm{T}}$ for the AD reaction $\mathrm{H}^- + \mathrm{H} \rightarrow \mathrm{H}_2 + \mathrm{e}^-$. The solid dots are the result of our extended cross section calculation based on the method developed in (*S10*). The cross section has been multiplied with the relative velocity and convolved with a Maxwell-Boltzmann velocity distribution. The black line is a plot of the analytical fit given in Table 1. The Langevin rate constant is plotted as a dashed black line. The previous theoretical results of Browne and Dalgarno for two different potentials are given as red solid and dashed lines, respectively (*S14*). The calculations of Sakimoto are shown as a blue line (*S15*). The calculations of Launay *et al.* for two different potentials are shown as green solid and dashed lines, respectively (*S16*). The room temperature (300 K) flowing afterglow results of Schmeltekopf *et al.* (*S11*), Fehsenfeld *et al.* (*S12*), and Martinez *et al.* (*S13*) are plotted as black squares at 250 K, 300 K, and 350 K, respectively.

Table S1: Parameters for the fit to the thermal rate coefficient $\alpha_T$ for reaction 1 (in units of $cm^3s^{-1}$, with temperature in K). The fit function is $\alpha_T = c_1(T^{c_2} + c_3T^{c_4} + c_5T^{c_6})/(1 + c_7T^{c_8} + c_9T^{c_{10}} + c_{11}T^{c_{12}})$. The fit reproduces our theoretical cross section results multiplied with the relative velocity and convolved with a Maxwell-Boltzmann velocity distribution to better than 3% (maximum discrepancy) for temperatures from $10^{-1}$ to $10^5$ K. Based on the strong agreement with the experimental results, we recommend this fit for the thermal rate coefficient of the AD reaction. We estimate an absolute $1\sigma$ uncertainty of 25%, corresponding to the systematic uncertainty of the experiment.

| $i$ | $c_i$ |
|---|---|
| 1 | 1.3500E-09 |
| 2 | 9.8493E-02 |
| 3 | 3.2852E-01 |
| 4 | 5.5610E-01 |
| 5 | 2.7710E-07 |
| 6 | 2.1826E+00 |
| 7 | 6.1910E-03 |
| 8 | 1.0461E+00 |
| 9 | 8.9712E-11 |
| 10 | 3.0424E+00 |
| 11 | 3.2576E-14 |
| 12 | 3.7741E+00 |